Climatological patterns over South America derived from COSMIC radio occultation data

R. Hierro,[1] P. Llamedo,[1] A. de la Torre,[1] P. Alexander,[2] and A. Rolla[1]

[1]   Meteorological phenomena are closely linked to the presence of water vapor. They mainly originate and develop in the troposphere, where almost all the atmospheric water is concentrated. The Global Positioning System radio occultation (GPS RO) technique provides vertical profiles of refractivity from which other properties such as temperature and water vapor can be derived. The GPS RO capability to reproduce global, synoptic, and regional climatological patterns over South America, which is a mostly oceanic continent, is tested. From FORMOSAT-3/COSMIC mission data (2006–2010), our previous knowledge regarding global and synoptic/regional patterns of temperature, equivalent potential temperature, specific humidity, and pressure is verified. Special cases such as baroclinic disturbances arriving at South American midlatitudes and storm events over a mountain region near the Andes are analyzed. The temporal evolution and the latitude-longitude distribution in several layers of the variables listed above are well described with this technique.

Citation: Hierro, R., P. Llamedo, A. de la Torre, P. Alexander, and A. Rolla (2012), Climatological patterns over South America derived from COSMIC radio occultation data, *J. Geophys. Res.*, *117*, D03116, doi:10.1029/2011JD016413.

1.   Introduction

[2]   Water vapor is one of the most important variables in the troposphere because of its influence in the energy transport and circulation within the Earth weather and climate system through latent heat exchange. Besides, it is the most important greenhouse gas in the atmosphere. Water vapor largely affects the radiative balance of the Earth surface and the extent and type of the continental biosphere.

[3]   For decades, the radiosonde network has provided all-weather in situ water vapor measurements but in a very limited and inhomogeneous area. Nowadays, satellite instruments provide high-resolution humidity profiles with global coverage. In particular, the Global Positioning System (GPS) radio occultation (RO) technique is a powerful tool to study the global distribution of water vapor with a moderate/high spatial and temporal resolution. The GPS RO technique provides vertical profiles of atmospheric properties such as refractivity, from which density (ρ), pressure (P), temperature (T) and water vapor pressure (e) are derived. The Constellation Observing System for Meteorology Ionosphere and Climate/Formosa Satellite 3 (hereafter referred to as COSMIC) mission provides about 1800 daily RO profiles with almost uniform global coverage. The vertical resolution of RO profiles ranges from 0.2 km in the lower troposphere to 1.4 km in the stratosphere [*Kursinski et al.*, 1997].

However, COSMIC post processed profiles are available from near the surface to up to 40 km, interpolated every 0.1 km. The "open-loop" mode tracking routine [*Anthes et al.*, 2008] used in COSMIC retrievals significantly reduces the inversion biases by eliminating tracking errors [*Sokolovskiy et al.*, 2007], extending those retrievals deeper into the lower troposphere. In the "open loop" mode, more than 90% of COSMIC soundings penetrate to the lowest 2 km of the troposphere [*Ho et al.*, 2010]. It is important to note that additional meteorological information is required to derive e in the middle and lower troposphere. COSMIC uses the 1D-Var method technique [*Healy and Eyre*, 2000] to retrieve both e and T profiles. 1D-Var method is an effective way to combine information provided by GPS RO and a priori atmospheric state (ECMWF T, P and e data) in a statistically optimal way. *Ho et al.* [2010] compared the specific humidity profiles derived from COSMIC with those of global ECMWF analysis over different regions, during both day time and nighttime, and found an almost zero mean bias. *Kishore et al.* [2011] studied the distribution of water vapor between 50°S and 50°N observed by COSMIC and compared it with radiosonde data sets. A good agreement was found, up to 8 km suggesting that COSMIC water vapor data are reliable in the troposphere. This shows the usefulness COSMIC water vapor profiles as an independent reference for quantifying humidity uncertainties among different sensors. This work is motivated by the insufficient measurements from other sources over South America. The aim is to evaluate the capability of GPS-RO to represent tropospheric processes throughout different meteorological fields. The latter are widely associated to water vapor, which is mostly concentrated in the lower troposphere. In section 2, regional

[1]Facultad de Ingeniería, Universidad Austral, Buenos Aires, Argentina.
[2]Departamento de Física, Facultad de Ciencias Exactas y Naturales, Universidad de Buenos Aires, Buenos Aires, Argentina.
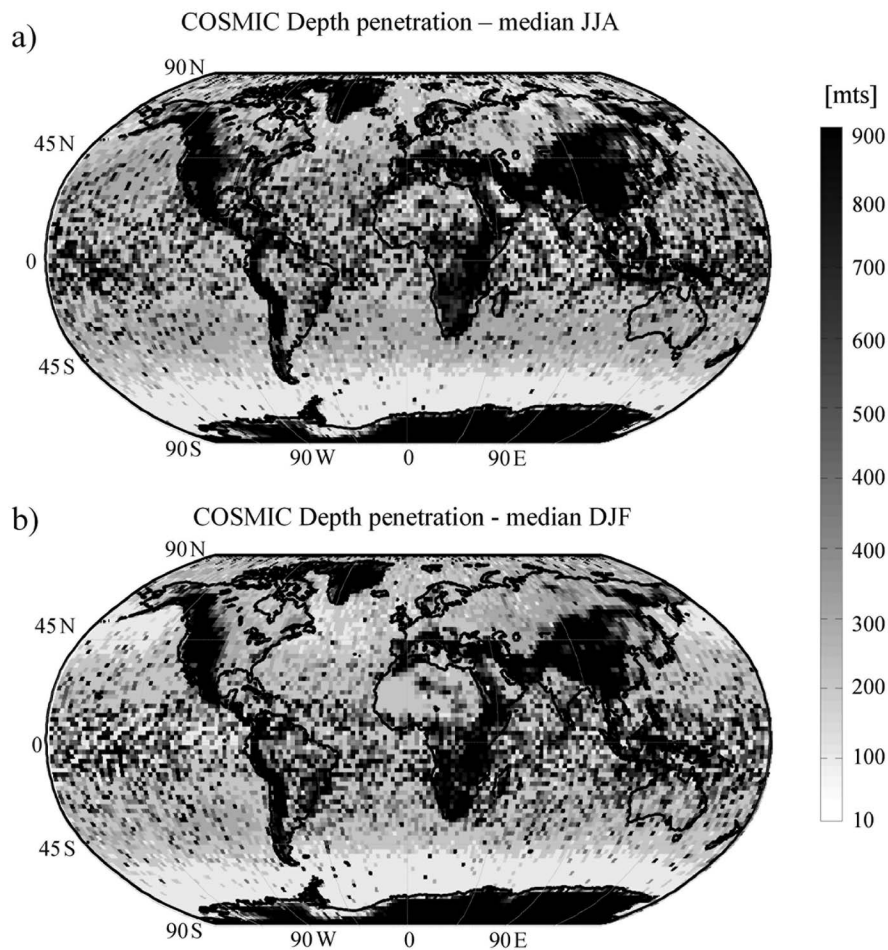
Figure 1. Median of the depth penetration for COSMIC data during 2006–2010 for (a) June–August (JJA) and (b) December–February (DJF) in 1° × 1° cells.

features of South America are introduced. In section 3, a COSMIC RO data (2006–2010) description and the methodology employed are presented. In section 4, the global distribution of low-level specific humidity and time evolutions over selected areas are examined and the synoptic/regional fields over South America are presented and discussed.

2. Regional Characteristics

[4] South America is characterized by its large oceanic area and its unique topography, which consists in a north-south barrier with tops up to 7 km, from the equator to 55°S, blocking the zonal flow over the Southern Hemisphere and impacting the regional circulation by determining the position of the planetary waves [*Seluchi et al.*, 2003]. According to *Zhou and Lau* [1998], the South American Monsoon System (SAMS) starts its development during spring over South America. This is featured by a southward shift in convection, dominant over the highland region of the central Andes and Amazonia and merging with the South Atlantic Convergence Zone (SACZ), while the Intertropical Convergence Zone (ITCZ) in the eastern Pacific and western Atlantic, is weakened. As stated by *Vera et al.* [2006], SAMS exhibits a surface low pressure and an upper level

anticyclone with seasonal changes in precipitation (increases and decreases) associated to an intense low-level inflow of moisture into the continent. This is under the dynamical influence of the Andes, which favors a poleward flow east of them all the year [*Nogués-Paegle et al.*, 1998]. The regional circulation over the south of South America has been studied by several authors: the summer continental heating gives rise to the formation of a quasi-permanent low-pressure system over the Chaco region (between Paraguay and Bolivia) which extends meridionally on the lee side of the Andes, from the Amazon to northwestern Argentina [*Seluchi et al.*, 2003]. On the other hand, *García-Ortega et al.* [2009] mentioned that this part of the continent shows a high frequency of severe convective storms with intense precipitation, large hailstones, damaging winds and occasional tornados. They pointed out that in this setting, the combination of subsynoptic factors such as diurnal warming, convective instability, and moisture flux convergence, may trigger mesoscale convection. Several authors have noted a maximum in the low-level moisture about 30°S–40°S during the austral summer, associating this enhancement with the deep convection in the region [*de la Torre et al.*, 2004; *Simonelli et al.*, 2007; *Teitelbaum et al.*, 2008]. *Velasco and Fritsch* [1987] surveyed the mesoscale convective complexes (MCCs) over South America using Geostationary Operational
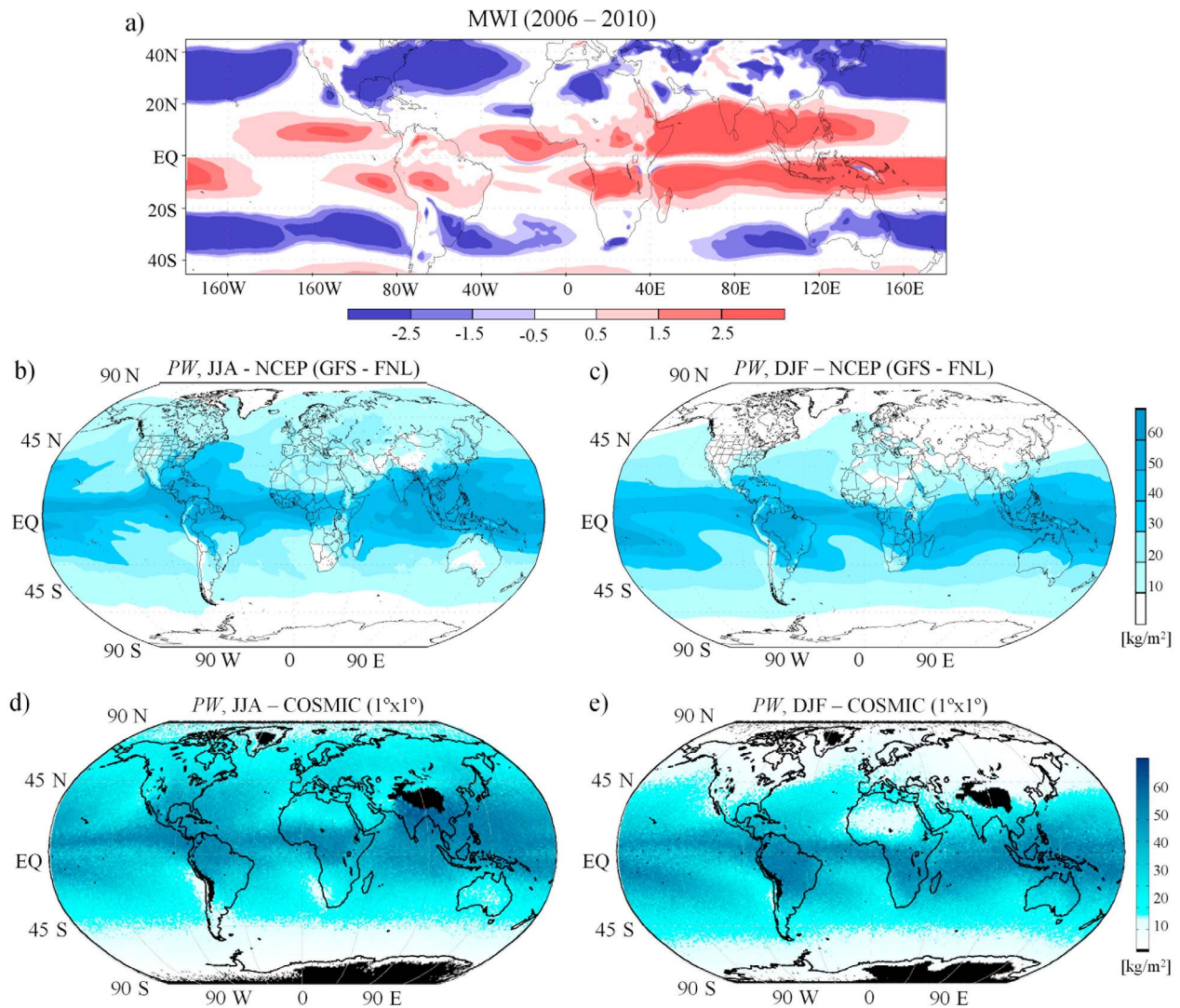
Figure 2. (a) Monsoon westerly index (*MWI*) for the whole period 2006–2010. Red areas indicate *MWI* > 0.5. Precipitable water (*PW*) from the National Centers for Environmental Prediction (NCEP; GFS-FNL) data for (b) JJA and (c) DJF and derived from COSMIC GPS radio occultation (RO) for (d) JJA and (e) DJF.

Environmental Satellite (GOES) infrared imagery, and found a large population of such complexes over the east of the continent between 20° and 40°S, especially during December and January. Those MCCs tend to develop during the evening and reach their maximum size after midnight. In this respect, two useful variables to evaluate this situation are specific humidity (*q*) and the equivalent potential temperature (θ_e). While the former gives information about the water vapor, the latter constitutes a good measure of heat and moist air content in an air parcel.

3. Data Set and Methodology

[5] COSMIC postprocessed level 2 "wet" data provide *T*, *P*, and *e* vertical profiles from near the surface up to 40 km, interpolated every 0.1 km. COSMIC data are binned into longitude, latitude, altitude and time grid cells and then averaged using different grid cell sizes, according to the process shown below.

[6] From COSMIC data, the specific humidity (*q*) is calculated as

$$q = \frac{w}{1 + w} \qquad (1)$$

where $w = 0.622\frac{e}{P-e}$ is the water vapor mixing ratio. Then, the equivalent potential temperature (θ_e) is calculated as

$$\theta_e \equiv \left(T + \frac{L_v}{c_p}w\right)\left(\frac{P_0}{P}\right)^{\frac{R_d}{c_p}} \qquad (2)$$

where R_d is the specific gas constant for air, L_v is the latent heat of evaporation and c_p is the specific heat of dry air at constant pressure. By definition, θ_e allows differentiating two
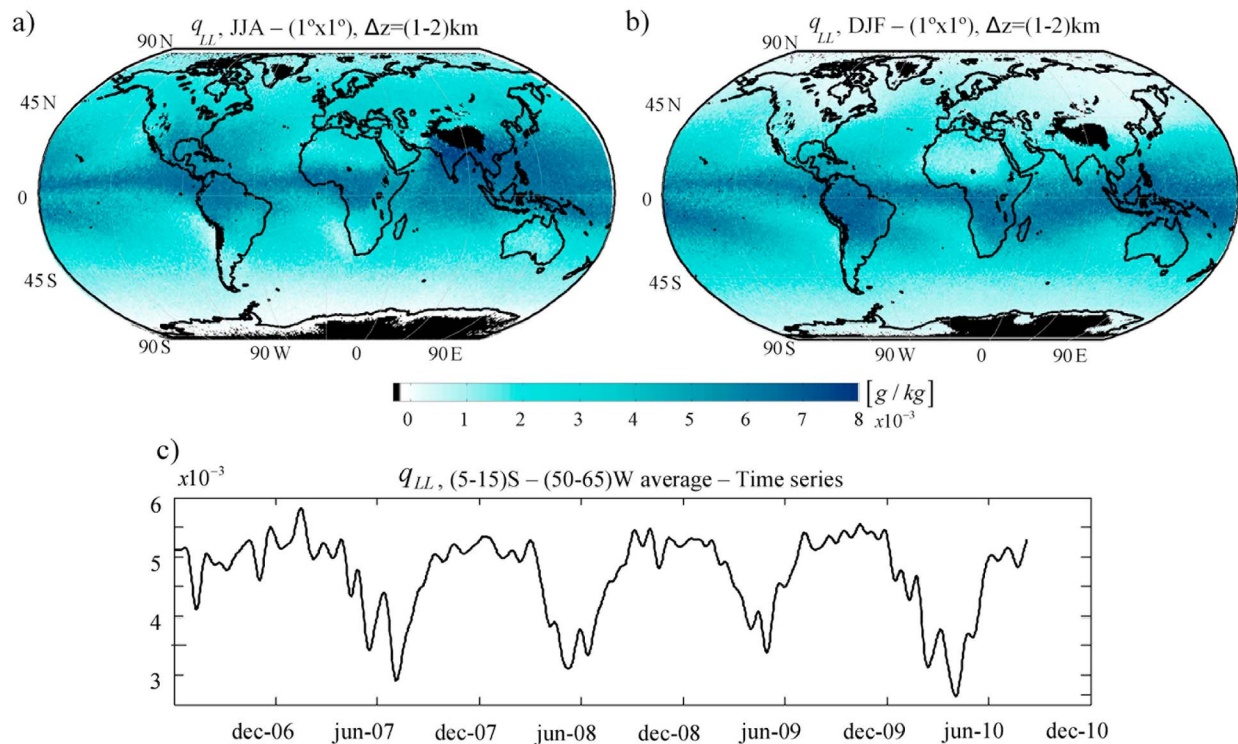
Figure 3. The 1–2 km averaged specific humidity with $1° \times 1°$ horizontal resolution for (a) JJA and (b) DJF. Black regions indicate there are no available GPS RO data. (c) Time evolution of q_{LL} (smoothed, see text) over the tropical Amazon region (see text) for the 2006–2010 period.

air masses: warm, wet and cold, dry. It is useful to recognize baroclinic zones, where a strong contrast in θ_e may indicate the presence of a cold/warm front. Taking into account that COSMIC data are available at constant height (instead of pressure), we consider as "low levels" those averaged between two heights of the lower troposphere, typically 500–600 hPa. Hereinafter, the variables will be referred to "low levels" (subindexes LL) when they are averaged between 1 and 2 km ($\approx$ 850–800 hPa under the hydrostatic approximation). Note that if the lower-altitude datum of a given profile is more than 1 km, the average is considered between this altitude and 2 km. Figure 1 shows the median global distribution of the depth penetration (lower-altitude data). In South America, the median values are higher than 1 km over the Andes and the Brazilian Plateau.

4. Results

4.1. The q_{LL} Global Fields

[7] In this section, the capability of the GPS RO technique to reproduce the global averaged total atmospheric water vapor content as well as the distribution of q_{LL} is evaluated. The total atmospheric water vapor contained in a vertical column is well represented by the precipitable water (PW), defined as $PW = \frac{1}{g} \int_{P_s}^{P_t} w\,dp$, where g is the acceleration of gravity and P_s and P_t are the pressure at the surface and at the top of the atmosphere, respectively. We compare this variable obtained from COSMIC GPS RO data with NCEP FNL (National Centers for Environmental Prediction (final) global gridded analysis archive), with $1° \times 1°$ horizontal

resolution and 27 verticals vertical levels. We focus on the monsoon regions, where rapid water vapor exchanges take place. As stated by *Wang and Ding* [2008], the monsoon climate is characterized by an annual reversal of the low-level winds. Following their methodology, the monsoon regions are detected using the monsoon westerly index (MWI) which is defined as $MWI = \frac{u_{850}^{MS} - u_{850}^{NM}}{\bar{u}}$ for the Northern Hemisphere and $MWI = \frac{u_{850}^{NM} - u_{850}^{MS}}{\bar{u}}$ for the Southern Hemisphere, where u_{850}^{MS} and u_{850}^{NM} are the 850 hPa zonal wind averaged from May to September and from November to March, respectively, and $\bar{u}$ is the annual mean of the zonal wind. Figure 2a shows the monsoon domain (red shaded areas) as depicted by MWI (2006–2010), when its value is greater than 0.5. While the tropical Asian-Australia-African monsoon regions are very well distinguished, the American monsoons are weak in terms of annual reversal of zonal winds, but still discernible [*Wang and Ding*, 2008]. Figures 2b and 2c show PW from NCEP data, while COSMIC data seasonally averaged is shown in Figures 2d and 2e. The enhancements present in NCEP data (Figures 2b and 2c) are also observed in PW derived from GPS RO (Figures 2d and 2e), showing high values over the $MWI > 0.5$ regions (Figure 2a) and low values, for example over Northern Africa during DJF and Australia, Southwestern Africa and West of South America during JJA. Figures 3a and 3b show q_{LL} for JJA and DJF, respectively. It is possible to observe low values over the extratropical regions during winter in each hemisphere. In both seasons, high values are present over the equator. During JJA, the highest concentrations are found over the western side of the Pacific Ocean,
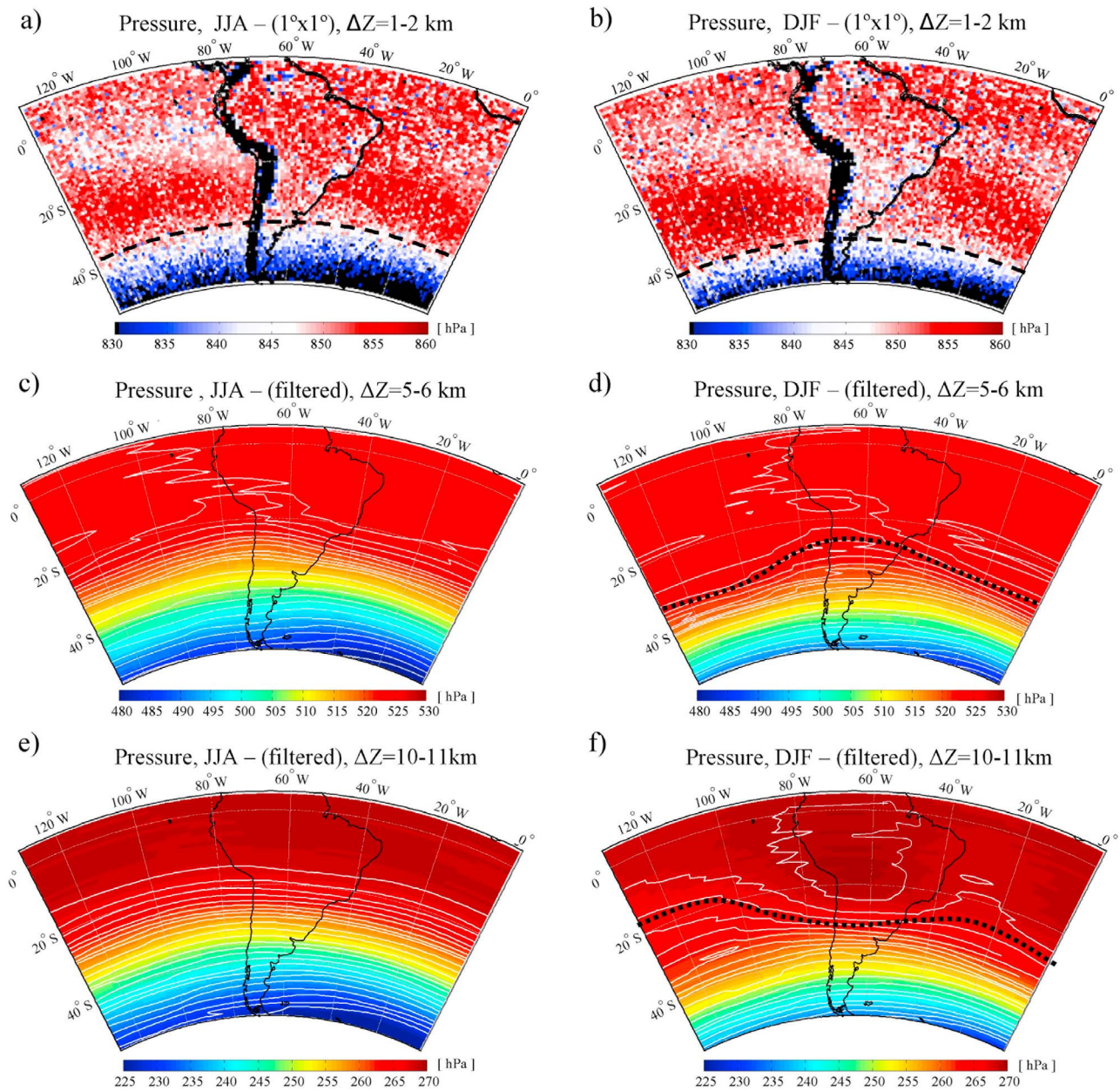
Figure 4. P_{LL} from COSMIC data, with $1° \times 1°$ horizontal resolution, for (a) JJA and (b) DJF. Dashed lines indicate the transition between high and low pressure according to the scale employed. (c) JJA and (d) DJF midlevel pressure (smoothed). (e) JJA and (f) DJF upper level pressure (smoothed). Dotted lines indicate the midlevel trough and the upper level ridge.

India and Indian Ocean, southern Asia and central Africa and during DJF, over the Indian Ocean, northern Australia, Indonesia and Brazil. These results are in agreement with those previously shown by *Kishore et al.* [2011] and *Chou et al.* [2009]. In the first one, the mean q distribution derived from COSMIC data during JJA and DJF between 2006–2009 are compared with JRA-25 and ERA-Interim data. In the second one, COSMIC humidity data are compared with AIRS retrievals and NCEP/NCAR reanalyses. As stated by *Vera et al.* [2006], during DJF there is an increase in the vertically averaged climatological mean moisture flux over the tropical and central Amazon. On the basis of this, the

seasonal evolution of q_{LL} over the region 5°–15°S, 50°–65°W is shown in Figure 3c. Here a monthly average is applied to smooth the signal. For the period June 2006 to June 2010, the decreasing/increasing q_{LL} values during JJA/DJF, are clear. The differences between both seasons are almost 50%, reaching values of 5.5–6×10^{-3} g/kg during summer and falling to values that are close to 3×10^{-3} g/kg during winter.

4.2. Synoptic-Scale Fields

[8] Following the traditional methodology of weather analysis, which considers a two layers tropospheric model,
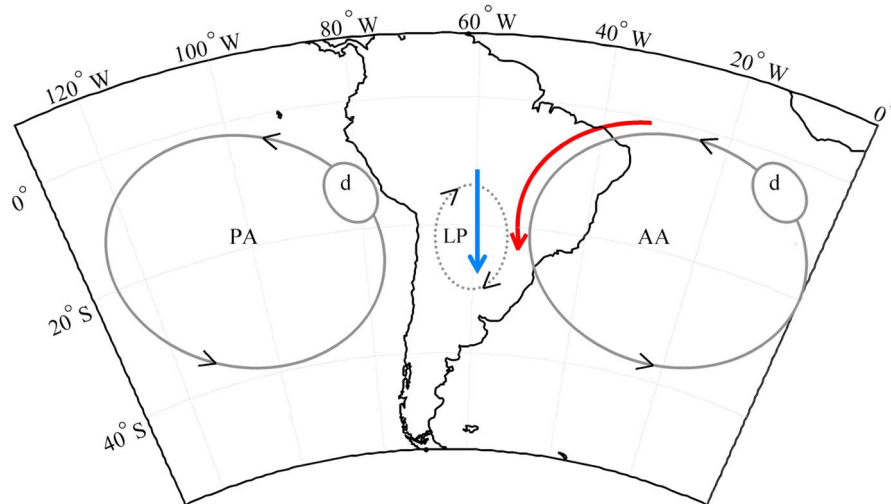
Figure 5. Schematic representation of the low-level circulation during DJF. The arrowheads over AA and PA indicate the systems circulation. The arrows over LP and AA schematize the resultant low-level circulation. AA, Atlantic anticyclone; PA, Pacific anticyclone; LP, low-pressure system (Chaco Low); d, dry zones.

we reproduce here the low, middle and upper levels fields. The P_{LL} patterns for DJF and JJA are shown in Figures 4a and 4b. The climatological positions of the Pacific and Atlantic semipermanent anticyclonic systems are evident during both seasons [*Garreaud and Wallace*, 1997]. As expected, the two systems are intensified during DJF, accompanied by a southward displacement. Taking the average between 37° and 40°S over the Pacific Ocean (120°–80°W) and Atlantic Ocean (45°–5°W), the mean pressure values during JJA are ≈847 and ≈844 hPa, respectively. During DJF there is a clear increase in these variables, reaching values of 857 and 853 hPa over those regions. Here a considerable difference appears between the two seasons along these latitudes, with higher values during summer. The inferred low-level circulation from Figures 4a and 4b is analogous to that described by other authors [e.g., *Campetella and Vera*, 2002] and is illustrated in Figure 5. Here a northerly flow is produced by the counterclockwise circulation associated to the South Atlantic anticyclone and a relative low-pressure system developed over the center and south of the continent, known as Chaco Low (CHL) [*Seluchi et al.*, 2003]. In Figure 5, the circulation associated to each pressure system is marked with arrows over PA, LP, and AA regions, while each individual contribution over the central part of the continent is indicated with (1) the central arrow (over LP) and (2) the bent arrow (on AA). The CHL is a thermal system, and therefore, it weakens with increasing height and reverses in the upper level [*Seluchi et al.*, 2003, and references therein]. Even though it is present in the annual mean field, it is intensified during DJF [*Seluchi and Marengo*, 2000]. Figures 4c and 4d show midlevel pressure fields (smoothed and averaged in 5–6 km) for both seasons. As described above, Figure 4d indicates that during DJF a longwave trough over the CHL is present at midlevel, while at the upper level, it reverses to form a ridge (see dotted lines in Figures 4d and 4f). Taking the average in this field between 20° and 30°S over the Pacific Ocean (120°–80°W), the continent (80°–45°W), and the Atlantic Ocean

(45°–5°W), the mean pressures obtained are ≈523, ≈520, and ≈523 hPa, respectively. We see here an absolute difference of −3 hPa between the central region and both sides. From upper level fields, it is possible to observe that the midlevel trough reverses to form a ridge (see dotted lines in Figures 4d and 4f). In this layer, the mean pressure averaged between 20° and 30°S is around 265 hPa over the Pacific Ocean (120°–80°W), 267 hPa over the Atlantic Ocean (45°–5°W), and 270 hPa over the continent (80°–45°W). Thus, an absolute difference of +4 hPa between the central region and both sides is obtained, showing the presence of a ridge over the continent. Other aspects observed at upper level are (1) the northward JJA displacement of the systems at midlatitudes, (2) the high-pressure system known as Bolivian High (BH) centered about 10°S, which is the dominant South America upper-level circulation feature, and (3) the presence of a strong ridge to the east, between 20° and 40°W, known as the Northeast High. Both points 2 and 3 are well described by *Lenters and Cook* [1997].

[9] Figures 6a and 6b show $\theta_{e(LL)}$ for both seasons. During JJA (Figure 6a), low values of $\theta_{e(LL)}$ are located from the central to the southern region over the continent. Mean values of 313 and 337 K during JJA and DJF, respectively, are seen. For example, taking the average between 25° and 35°S, $\theta_{e(LL)}$ mean values are 310, 313, and 313 K over the Pacific Ocean (120°–80°W), the continent (80°–45°W), and the Atlantic Ocean (45°–5°W) respectively, resulting in a slight absolute difference of 3 K over the whole domain. During DJF (Figure 6b), a zonal maximum at midlatitudes is observed over the continent, yielding to the presence of a warm and wet "tongue" over the north and center of Argentina. In this case, the average of mean values of $\theta_{e(LL)}$ between 25° and 35°S are 322, 337, and 325 K over the Pacific Ocean (120°–80°W), the continent (80°–45°W,) and the Atlantic Ocean (45°–5°W), respectively, showing a clear increase of wet and warm air over the continent.

[10] The synoptic scale q_{LL} for both seasons is presented in Figures 6c and 6d. During JJA, lower values are observed
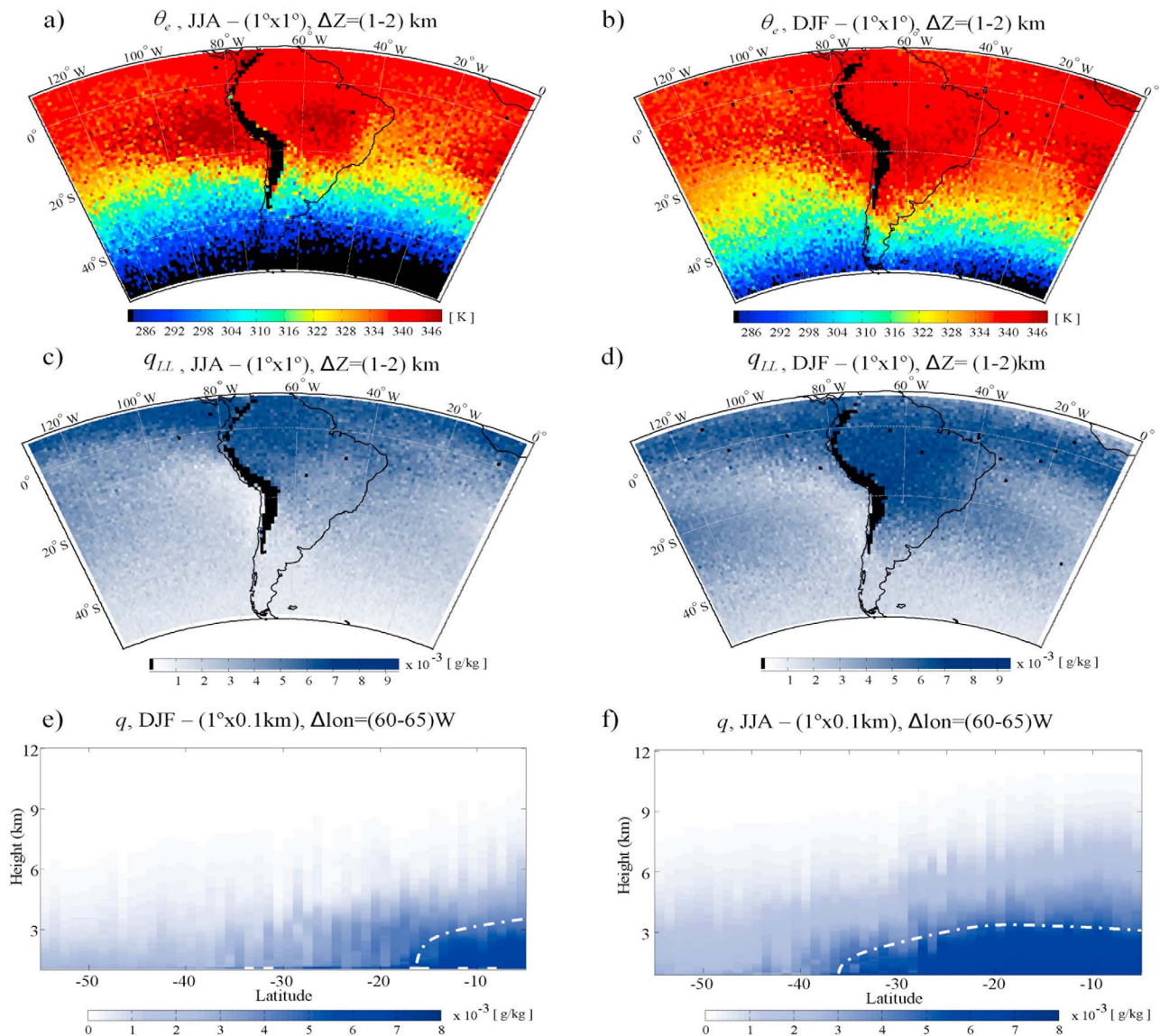
Figure 6. Plots showing $\theta_{e(LL)}$ over South America for (a) JJA and (b) DJF, q_{LL} corresponding to (c) JJA and (d) DJF, and q Z-lat slices for (e) JJA and (f) DJF from 0 to 12 km. Dash-dotted line marks a moist core over South America in both seasons.

over the whole continent (Figure 6c), with a maximum region over the equator, extending toward central South America. During DJF (Figure 6d), higher values are present over the whole continent and the area containing the maximum is located south of the equator, over the Amazon and decreasing toward the north of Argentina. At midlatitudes, a relative maximum over the continent is present, probably associated with a warm and wet air transport from lower to higher latitudes, whose associated inflow was described by *Seluchi and Marengo* [2000] and *Garreaud* [2009]. From q_{LL}, the presence of both the Pacific and Atlantic anticyclones is more evident during DJF, with low values over the eastern branches of the two systems (see detail, labeled d, in Figure 5), which are typically dry zones in maritime tropical air masses [*Petterssen*, 1941]. These JJA and DJF patterns match those described in several studies for other variables, such as outgoing longwave radiation, precipitation or cloud

distribution over South America [e.g., *Marengo et al.*, 2004; *Vera et al.*, 2006]. The vertical structures of specific humidity are analyzed in Figures 6e and 6f which show vertical slices of longitudinal averages (hereinafter Z-lat slices) between $60°$ and $6°5W$ for both seasons. The presence of a low-level moist core centered over the equator is clear during JJA (Figure 6e), showing high values up to 15°S, and decreasing toward the south. During DJF (Figure 6f), an increase of this variable is observed between 15° and 35°S and the moist core is displaced toward the pole, centering about 15°–20°S. At those latitudes, it is possible to localize its major vertical extension, reaching altitudes of 8–9 km, with values $\approx 3 \times 10^{-4}$ g/kg.

4.3. Time Evolution

[11] The q_{LL} seasonal feature observed over Argentina (25°–55°S, 70°–55°W) in Figures 6c and 6d, as well as the
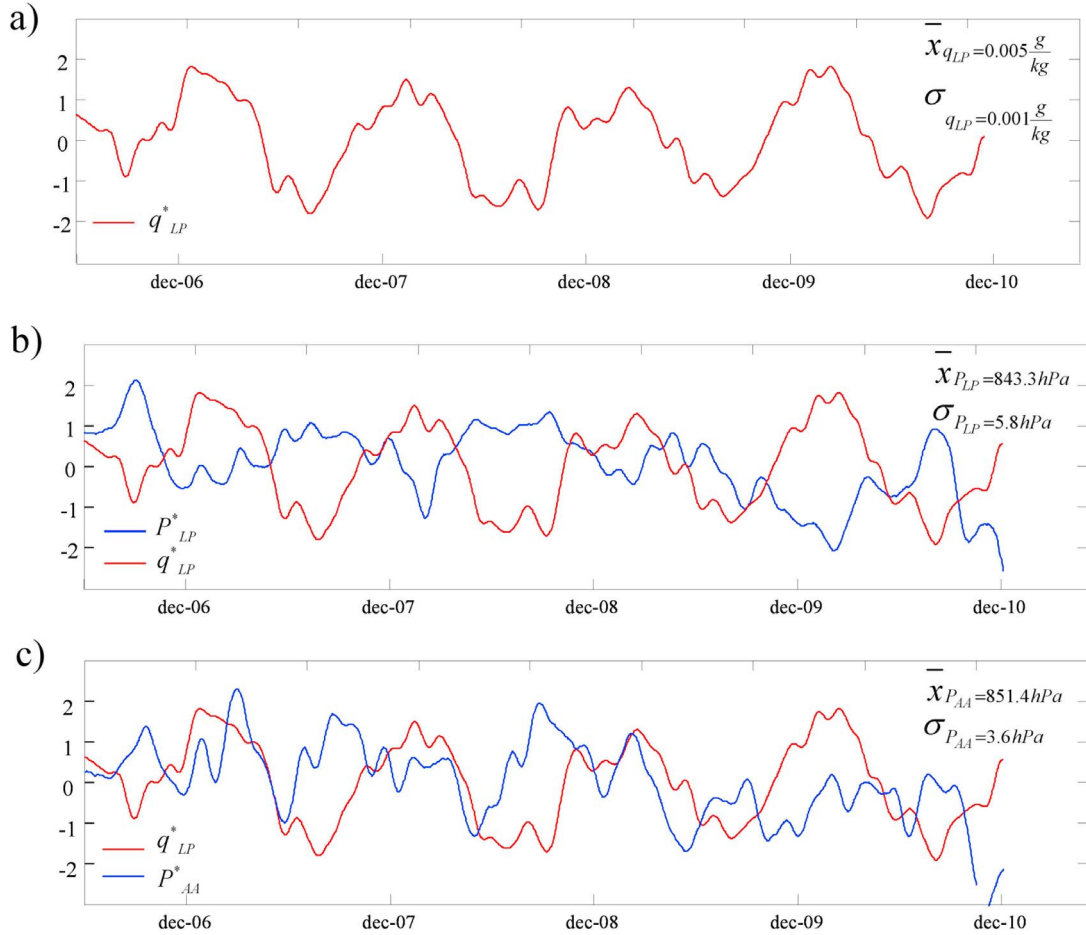
Figure 7. The 2006–2010 smoothed and standardized 2006–2010 time evolutions of (a) q_*^{LP} over the LP region, (b) the same as Figure 7a for q_*^{LP} and P_{LL} (P_*^{LP}), and (c) the same as Figure 7a for q_*^{LP} and P_{LL} over the AA region (P_*^{AA}).

low-level circulation associated with P_{LL}, were evaluated from the time evolution analysis of both variables. The methodology employed is as follows: (1) Two regions were selected: one located over Argentina with coordinates 20°–35°S, 55°–69°W (hereinafter LP), which covers the influence zone of the low-pressure system represented in Figure 5, and another over the Atlantic Ocean, covering the Atlantic anticyclone influence zone (hereinafter AA), with the coordinates 20°–40°S, 10°–30°W. (2) The time evolution of q_{LL} and P_{LL} in LP and AA were obtained and then, in order to retain only the synoptic-scale fluctuations, a low-pass band filter was applied to each variable. (3) To allow the comparison between them, the resulting signals were then standardized:

$$P_* = \frac{P_{LL} - \overline{P_{LL}}}{\sigma_P}, q_* = \frac{q_{LL} - \overline{q_{LL}}}{\sigma_q} \qquad (3)$$

where $\overline{P_{LL}}, \overline{q_{LL}}, \sigma_P, \sigma_q$ are the corresponding mean value and standard deviation for each variable. The joint evolutions of P_* and q_* over LP and AA were analyzed. These results are presented in Figure 7. Here q_*^{LP} (Figure 7a) shows the same

behavior observed in Figure 3c for q_{LL} over the tropical Amazon region (see section 4.1), with low values during JJA and high values during DJF. As stated above, during DJF a low-pressure system (Chaco Low) deepens over Argentina. At this time, P_*^{LP} (Figure 7b) shows decreasing values, while q_*^{LP} increases. During DJF, there is a 180° phase shift between both signals, being q_*^{LP} maximum while P_*^{LP} is minimum. In December 2009, this indirect behavior is also observed, although not so marked. Figure 7c shows the time evolutions of P_*^{AA} and q_*^{LP}. For the 2006, 2007, and 2008 signals a joint increase of the variables is observed, mostly during DJF. Although such increase is not so clear during DJF 2009, there is a P_*^{AA} minimum in December and after this, a slight increase, again in phase with q_*^{LP}. This is in consonance with the northern transport associated circulation described above (e.g., Figure 5) and with the results obtained from Figure 7b. All these features confirm the correspondence between the RO pressure fields and the known northern transport and low-level circulation over South America, as well as the capability of the technique to provide a good spatial synoptic variability of P and q, and their associated variables.
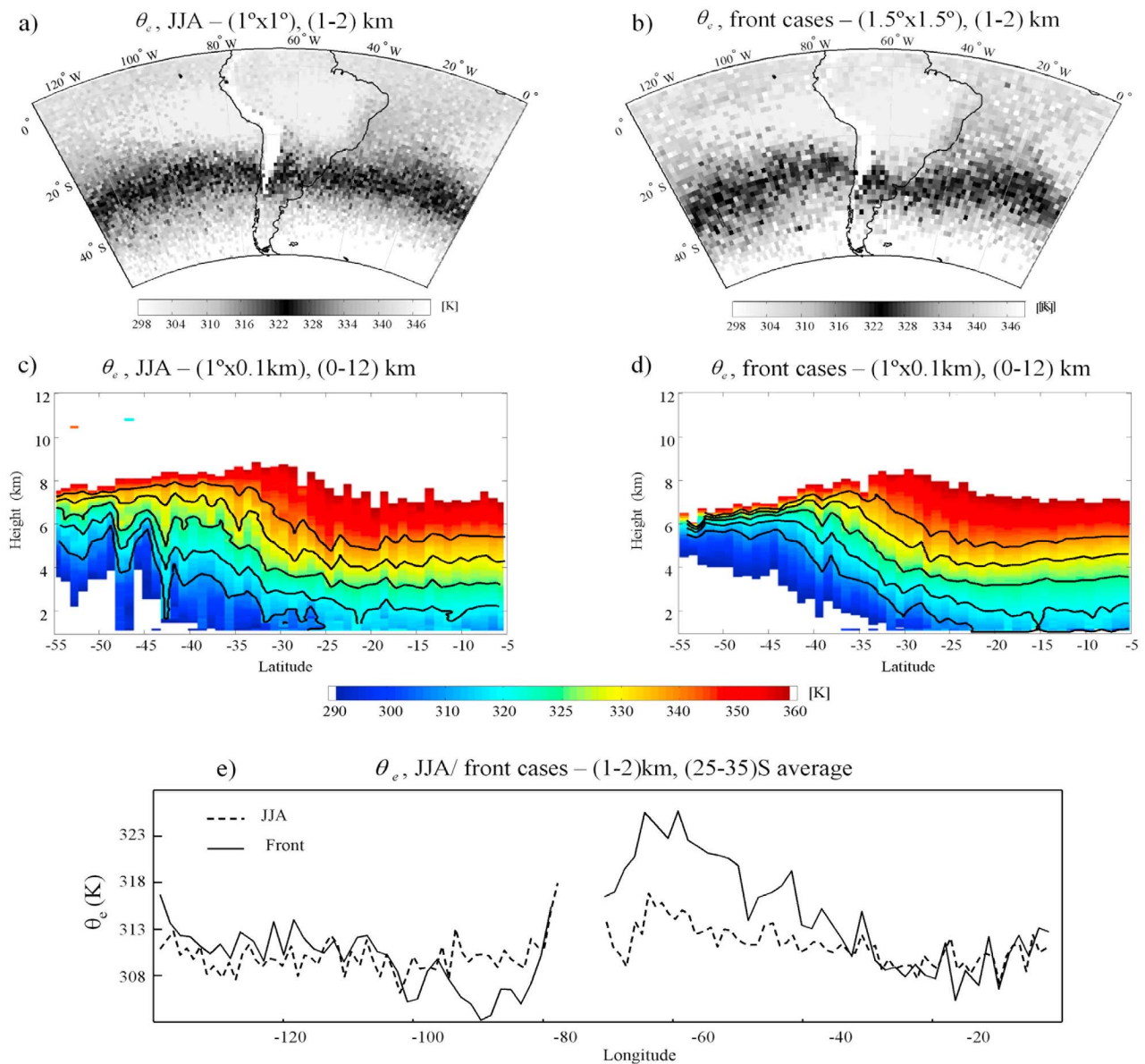
Figure 8. Plots showing $\theta_{e(LL)}$ for (a) the JJA season and (b) the front events during JJA. The strong contrast in $\theta_{e(LL)}$ is darkly shaded, (c and d) $\theta_{e(LL)}$ Z-lat slices for Figures 8a and 8b, and (e) $\theta_{e(LL)}$ for the JJA season (dashed line) and fronts events (solid line), averaged between 25°S and 35°S from 130°W to 0°W.

4.4. Regional Fields

[12] The south of South America is a baroclinic zone, where the front passages are abundant throughout the year the year and in particular during JJA. The central part of Argentina (south of 25°S) was selected to evaluate the capability to reproduce smaller scale meteorological phenomena: We considered (1) 40 events of cold front passages during JJA over the region for comparison with the JJA period averaged and (2) 43 events of severe hailstorms in Mendoza (Argentina) roughly located at 32°–36°S, 65°–69°W during 2006–2010 for comparison with the whole period averaged, respectively (see Appendix A). Here we take into account that it is possible to assume a normal distribution in both cases. Figures 8a and 8b depict $\theta_{e(LL)}$ for the

JJA period and for the 40 front events averaged, respectively. The dark zone indicates the transition zone between two air masses and, as expected, it is clearly marked in the frontal cases (Figure 8b) because of the stronger temperature contrast. Moreover, the baroclinic case is evident from the temperature field, showing the typical enhancement (along the dark region), and deviating the average $\theta_{e(LL)}$ from its JJA climatological zonal distribution (Figure 8a). Z-lat slices between 55° and 60°W for JJA and for the front cases are presented in Figures 8c and 8d, respectively. During JJA, south of 45°S, the 310 K contour is close to the 4 km height, while in front cases this isotherm reaches an altitude of almost 6 km, revealing the presence of colder air at lower levels over this region. It is possible to observe more differences between the two samples: a stronger temperature
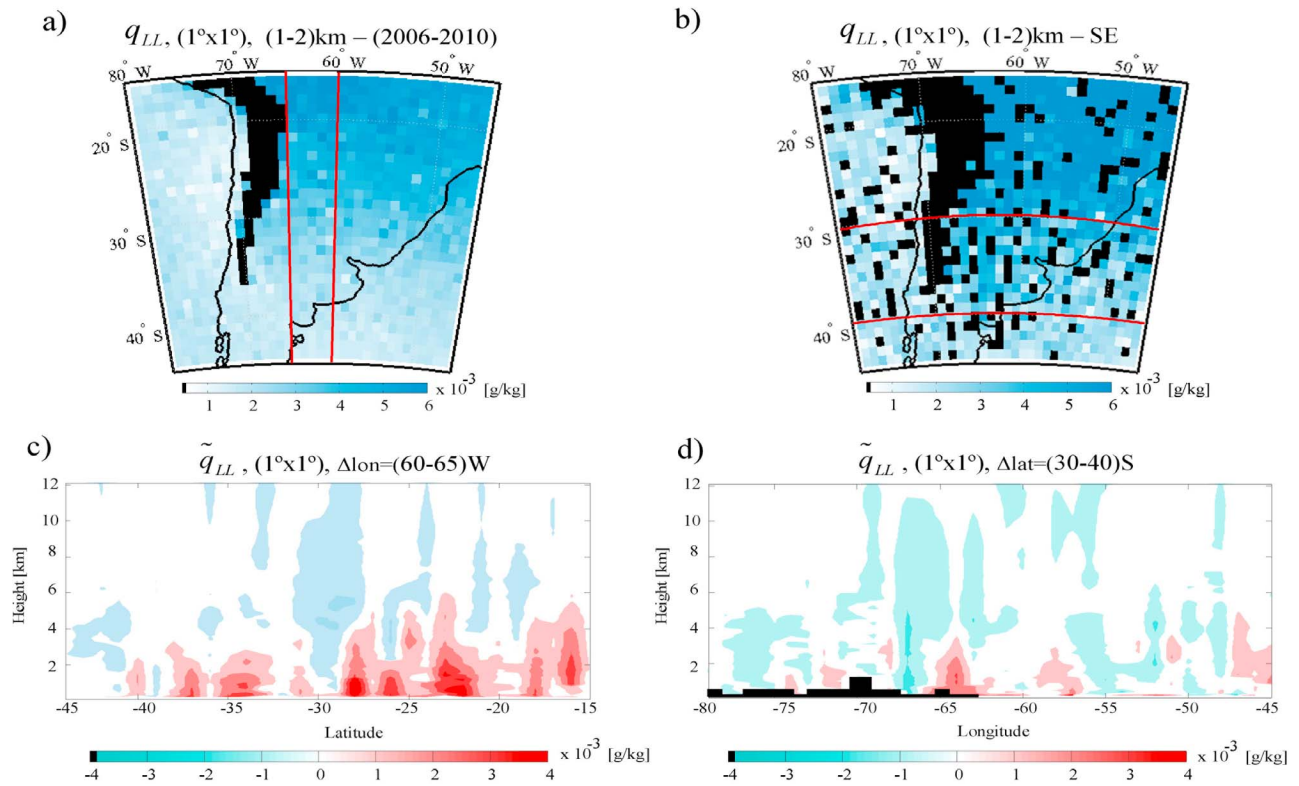
Figure 9. (a) The q_{LL} 2006–2010 period average and (b) q_{LL} averaged in storm events (SE); vertical slices of (c) longitudinal (60°W–65°W) and (c) latitudinal (30°S–40°S) averages of q_{LL} anomalies ($\widetilde{q}_{LL}$). The regions averaged in these slices are marked in Figures 9a and 9b with red lines.

contrast in the front cases (Figure 8d), depicted for the thinner contour separation, is evident from 35°S to higher latitudes. Toward the south, there is a marked presence of cold air on the basis of the low values of $\theta_{e(LL)}$ (white zone). South of 40°S, a contrast of about 1 K/100 km is present during winter, while in front cases this is about 5 K/100 km over the same region. In the JJA period, the temperature distribution presents a not so clear cold core at high latitudes and the meridional contrasts are not so marked (weaker contour separations). The feature present in Figures 8a and 8b is clearly observed in Figure 8e, which shows the 25°–35°S averaged mean $\theta_{e(LL)}$ for the whole domain in both samples. The front events (solid lines) present a larger amplitude than the winter cases (dotted line) between 90° and 40°W and are 5 K colder and 8 K warmer at the west and east sides of the Andes, respectively.

[13] Figures 9a and 9b present q_{LL} for the 2006–2010 period and the storm events (SE) average, respectively. In the SE case (Figure 9b) higher values of q_{LL}, when compared to those observed in the 2006–2010 frame (Figure 9a), are present over the north and the central zone of the domain. $\theta_{e(LL)}$ presents a positive anomalous area over the study region (not shown) indicating that, as expected in the case of SE, the GPS-RO data revealed a region dominated by a warmer and wetter air mass than the average. In Figures 9c and 9d we calculated the anomalies from $\widetilde{q}_{LL} = q_{LL}(SE) - q_{LL}$ (2006—2010). It makes $\widetilde{q}_{LL} > 0$ (< 0) when $q_{LL}(SE)$ is higher (lower) than q_{LL} 2006–2010 period. The features

mentioned above can be confirmed from Figures 9c and 9d, which show $\widetilde{q}_{LL}$ Z-lat between 60° and 65°W and Z-lon between 30° 40°S (red line in Figures 9a and 9b). From Figure 9d it is possible to observe, in general, positive values of $\widetilde{q}_{LL}$ at all latitudes and in particular, over the studied region at the south of 30°S, with two relative maxima near 34°–37°S. In the Z-lon slice (Figure 9d), higher values of $\widetilde{q}_{LL}$ are present at the east of the Andes over the region of interest, with a maximum close to 65°W. Clearly, the technique is indicating an increase of water vapor content in the storm events over Mendoza.

5. Conclusions

5.1. Global Fields

[14] 1. High values of PW over the monsoon regions ($MWI > 0.5$) and low values coinciding with the dry zones are obtained. A good correlation between PW COSMIC data and GFS model (2006–2010) during winter and summer in both hemispheres is verified.

[15] 2. Low values of q_{LL} over tropical regions during winter in both hemispheres and high values over the equator during both seasons are found. A coherent evolution over the tropical Amazon (in South America) is obtained, with low values during JJA and high values during DJF.

5.2. Over South America

[16] 1. At low level, the South Atlantic and South Pacific anticyclones are well represented, such as the thermal system

known as Chaco Low around 25°S, which intensifies during summer. At midlevel, a long-wave trough associated to the above mentioned system is clearly distinguishable. At the upper level, a high-pressure DJF pattern known as Bolivian High is centered at about 15°S, while to the south, a strong ridge is observed, probably associated with the inversion which occurs above to the Chaco Low.

[17] 2. The seasonal $\theta_{e(LL)}$ shows high values, incoming from the Amazon toward higher latitudes during DJF. It penetrates the north of Argentina, giving rise to the presence of a warm and wet tongue over this region. This $\theta_{e(LL)}$ distribution coincides with the inferred circulation from the P_{LL} fields mentioned above, which in turn show the same features described by other authors, in relation to the seasonal circulation over the continent. Similar features for q_{LL} are observed: vertical slices of longitudinal averages for both seasons confirm the presence of a moist core in 60°–65°W centered at low latitudes during JJA and extending toward the South covering midlatitudes during DJF.

[18] 3. The P_{LL} time evolution analysis at low-level over selected areas states a correlation between them, which coincides in the maximum with (1) the DJF northern circulation found in P_{LL} and in the (2) $\theta_{e(LL)}$ fields detected in this study and already described by other authors.

[19] 4. For 40 selected JJA front cases arriving at midlatitudes, $\theta_{e(LL)}$ derived from this technique exhibited an expected behavior, showing a withdrawal from the more barotropic case obtained for the JJA case. The baroclinic zone is clearly distinguishable at low level as well as in a vertical slice of longitudinal average between 55° and 60°W, where strong contrasts of $\theta_{e(LL)}$ are observed, allowing to locate the to locate the front position and its vertical structure.

[20] 5. Forty-three cases of hail storm events (SE) were selected over a mountain region near the Andes, between 32° and 36°S and 65° and 69°W, in order to analyze a smaller-scale performance of the technique. A comparison of q_{LL} between SE cases and the averages for the 2006–2010 period reveals that the expected increase in $\theta_{e(LL)}$ is present in SE over the studied region, while high values of q_{LL} are incoming from the north. Vertical slices of longitudinal and latitudinal averages anomalies show several peaks, which coincide in both cases with the area of SE occurrence.

[21] GPS RO data were demonstrated to be a useful tool, enabling estimation of prevailing atmospheric fields of relevance to climate in the lower and middle troposphere on not only global, but also regional scale (within South America).

Appendix A

[22] The 43 hailstorms database was provided by the government of Mendoza (http://www.contingencias.mendoza.gov.ar). The cold fronts database was obtained from the government of Mendoza and also verified from 2006–2010 NCEP data (FNL), considering the magnitude of $\frac{\partial T}{\partial x} > 3$ K/100 km as a flag of front cases and in addition, checking the low-level wind. Finally, we checked this information against official observations from the Argentinean National Meteorological Service (SMN; http://www.smn.gov.ar) available at http://www.ogimet.com, looking for a deep decreasing in temperature (over this region) at the dates found with the model data.

References

Anthes, R. A., et al. (2008), The COSMIC/FORMOSAT-3 mission: Early results, *Bull. Am. Meteorol. Soc.*, *89*, 313–333, doi:10.1175/BAMS-89-3-313.

Campetella, C., and C. Vera (2002), The influence of the Andes mountains on the South America low-level flow, *Geophys. Res. Lett.*, *29*(17), 1826, doi:10.1029/2002GL015451.

Chou, M.-D., C.-H. Weng, and P.-H. Lin (2009), Analyses of FORMO-SAT-3/COSMIC humidity retrievals and comparisons with AIRS retrievals and NCEP/NCAR reanalyses, *J. Geophys. Res.*, *114*, D00G03, doi:10.1029/2008JD010227.

de la Torre, A., D. Vincent, R. Tailleaux, and H. Teitelbaum (2004), A deep convection event above the Tunuyán Valley near to the Andes Mountains, *Mon. Weather Rev.*, *132*(9), 2259–2268.

García-Ortega, E., L. López, and J. L. Sánchez (2009), Diagnosis and sensitivity study of two severe storm events in the southeastern Andes, *Atmos. Res.*, *93*, 161–178.

Garreaud, R. (2009), The Andes climate and weather, *Adv. Geosci.*, *7*, 1–9.

Garreaud, R. D., and J. M. Wallace (1997), The diurnal march of the convective cloudiness over the Americas, *Mon. Weather Rev.*, *125*(12), 3157–3171.

Healy, S. B., and J. R. Eyre (2000), Retrieving temperature, water vapour and surface pressure information from refractive-index profiles derived by radio occultation data: A simulation study, *Q. J. R. Meteorol. Soc.*, *126*, 1661–1683.

Ho, S.-P., X. Zhou, Y.-H. Kuo, D. Hunt, and J.-H. Wang (2010), Global evaluation of radiosonde water vapor systematic biases using GPS radio occultation from COSMIC and ECMWF analysis, *Remote Sens.*, *2*, 1320–1330; doi:10.3390/rs2051320.

Kishore, P., M. Venkat Ratnam, S. P. Namboothiri, I. Velicogna, G. Basha, J. H. Jiang, K. Igarashi, S. V. B. Rao, and V. Sivakumar (2011), Global (50S-50 N) distribution of water vapor observed by COSMIC GPS RO: Comparison with GPS radiosonde, NCEP, ERA-Interim, and JRA-25 reanalysis data sets, *J. Atmos. Sol. Terr. Phys.*, *73*(13), 1849–1860, doi:10.1016/j.jastp.2011.04.017.

Kursinski, E. R., et al. (1997), Observing Earth's atmosphere with radio occultation measurement using the Global Positioning System, *J. Geophys. Res.*, *102*, 429–465.

Lenters, J. D., and K. H. Cook (1997), On the origin of the Bolivian high and related circulation features of the South American climate, *J. Atmos. Sci.*, *54*, 656–678.

Marengo, J., W. Soares, C. Saulo, and M. Nicolini (2004), Climatology of low-level jet east of the Andes as derived from the NCEP-NCAR reanalyses, *J. Clim.*, *17*, 2261–2280.

Nogués-Paegle J., K. Mo, and J. Paegle (1998), Predictability of the NCEP/NCAR reanalysis model during austral DJF, *Mon. Weather Rev.*, *126*, 3135–3152.

Petterssen, S. (1941), *Introduction to Meteorology*, 236 pp., McGraw-Hill, New York.

Seluchi, M., A. C. Saulo, M. Nicolini, and P. Satyamurty (2003), The northwestern Argentinean low: A study of two typical events, *Mon. Weather Rev.*, *131*, 2361–2378.

Seluchi, M. E., and J. A. Marengo (2000), Tropical-midlatitude exchange of air masses during DJF and JJA in South America: Climatic aspects and examples of intense events, *Int. J. Climatol.*, *20*, 1167–1190.

Simonelli, S., F. Norte, N. Heredia, and M. Seluchi (2007), The storm of January 1, 2000, north of the city of Mendoza, *Atmosfera*, *20*(1), 1–23.

Sokolovskiy, S. V., C. Rocken, D. H. Lenschow, Y.-H. Kuo, R. A. Anthes, W. S. Schreiner and D. C. Hunt (2007), Observing the moist troposphere with radio occultation signals from COSMIC, *Geophys. Res. Lett.*, *34*, L18802, doi:10.1029/2007GL030458.

Teitelbaum, H., H. Le Treut, M. Moustaoui, G. C. Cabrera, and G. Ibañez (2008), Deep convection east of the Andes Cordillera: A test case analysis of air mass origin, *Mon. Weather Rev.*, *136*, 2201–2209.

Velasco, I., and J. M. Fritsch (1987), Mesoscale convective complexes in the Americas, *J. Geophys. Res.*, *92*, 9591–9613.

Vera, C., et al. (2006), Towards a unified view of the American monsoon system, *J. Clim.*, *19*, 4977–5000.

Wang, B., and Q. Ding (2008), Global monsoon: Dominant mode of annual variation in the tropics, *Dyn. Atmos. Oceans*, *44*, 165–183, doi:10.1016/j.dynatmoce.2007.05.002.

Zhou, J., and K.-M. Lau (1998), Does a monsoon climate exist over South America?, *J. Clim.*, *11*, 1020–1040.

P. Alexander, Departamento de Física, Facultad de Ciencias Exactas y Naturales, Universidad de Buenos Aires, Ciudad Universitaria, 1428 Buenos Aires, Argentina.

A. de la Torre, R. Hierro, P. Llamedo, and A. Rolla, Facultad de Ingeniería, Universidad Austral, Avda. Garay 125, 5to Piso, C1063ABB Buenos Aires, Argentina. (rhierro@austral.edu.ar)